INTERNATIONAL JOURNAL FOR NUMERICAL METHODS IN FLUIDS
*Int. J. Numer. Meth. Fluids* 2001; **34**: 561–584

# Transient effects of orthogonal pipe oscillations on laminar developing incompressible flow

B. Benhamou, N. Galanis*,[1] and A. Laneville

*THERMAUS Research Group, Département de Génie Mécanique, Université de Sherbrooke, Sherbrooke, Québec, Canada J1K 2R1*

## SUMMARY

This paper presents a numerical study of the transient developing laminar flow of a Newtonian incompressible fluid in a straight horizontal pipe oscillating around the vertical diameter at its entrance. The flow field is influenced by the tangential and Coriolis forces, which depend on the through-flow Reynolds number, the oscillation Reynolds number and the angular amplitude of the pipe oscillation. The impulsive start of the latter generates a transient pulsating flow, whose duration increases with axial distance. In any cross-section, this flow consists of a pair of symmetrical counter-rotating vortices, which are alternatively clockwise and anti-clockwise. The circumferentially averaged friction factor and the axial pressure gradient fluctuate with time and are always larger than the corresponding values for a stationary pipe. On the other hand, local axial velocities and local wall shear stress can be smaller than the corresponding stationary pipe values during some part of the pipe oscillation. The fluctuation amplitude of these local variables increases with axial distance and can be as high as 50% of the corresponding stationary pipe value, even at short distances from the pipe entrance. Eventually, the flow field reaches a periodic regime that depends only on the axial position. The results show that the transient flow field depends on the pipe oscillation pattern (initial position and/or direction of initial movement). Copyright © 2000 John Wiley & Sons, Ltd.

KEY WORDS: fluid flow; laminar flow; oscillating pipe; transient flow

## 1. INTRODUCTION

The problem of fluid flow in a moving duct is encountered in many engineering applications, such as turbomachines and oscillating pipes in a ship. Movements such as uniform rotation about an axis either parallel or perpendicular to the main flow direction [1–3], oscillatory translation [4,5] or axial oscillations [6] have been studied numerically, analytically and experimentally. Most theoretical investigations deal with the fully developed laminar flow case and consider steady or fully established periodic conditions.

* Correspondence to: THERMAUS Research Group, Département de Génie Mécanique, Université de Sherbrooke, Sherbrooke, Québec, Canada J1K 2R1.
[1] E-mail: nicolas.galanis@gme.usherb.ca

*Received June 1999*
*Revised October 1999*

Our literature survey revealed that problems involving large amplitude, low frequency, radial duct oscillations about an axis perpendicular to the main flow direction have not been studied. This problem is of considerable theoretical interest and can have practical importance for internal flows in moving systems (road vehicles, ships, etc.). The pipe oscillations will induce a time-dependent transverse motion of the fluid. As established in other similar problems [3], this secondary motion can modify the axial velocity profile and increase pressure losses [7]. The resulting complex flow field is of considerable practical interest in heat/mass transfer devices, as it is expected to enhance the rate of both these phenomena.

The present study aims to establish the characteristics of the time-dependent, axially developing, laminar flow of an incompressible Newtonian fluid within a horizontal pipe, initially at rest, which is subjected to sinusoidal oscillations about a vertical axis for $t' > 0$ (with primed letters indicating dimensional variables). The pipe movement introduces the tangential and Coriolis forces in the momentum equations that describe the relative motion of the fluid with respect to the pipe. These forces, which depend on the direction of the oscillatory pipe movement and on the position of the fluid particles, result in a complex flow field structure. This structure depends on the values of three non-dimensional parameters: the through-flow Reynolds number, the oscillation Reynolds number and the amplitude of the pipe oscillations. The coupled non-linear, three-dimensional transient equations that describe this flow field have been solved numerically for different combinations of these three non-dimensional parameters [8,9].

In this paper we focus on the transient behaviour of the flow field following the impulsive initiation of the pipe oscillations. The motivation is to show and explain the effects of the pipe oscillations on some flow properties. In order to achieve this, a single combination of the problem parameters has been analysed for three different oscillation patterns. In all cases, the angular frequency of the oscillations is equal to the ratio of the mean axial velocity to the pipe diameter.

## 2. PROBLEM FORMULATION

Figure 1 shows a schematic representation of the system under study. An incompressible Newtonian fluid enters a straight circular pipe of constant diameter, which is initially stationary, with a uniform velocity $V_0$. At $t' = 0$, the pipe starts oscillating around its vertical diameter at $z' = 0$, with an angular velocity

$$\mathbf{\Omega} = \dot{\beta}\mathbf{y} = A\omega \cos(\omega t')\mathbf{y} \tag{1}$$

where the angular position of the pipe axis is

$$\beta = A \sin(\omega t') \tag{2}$$

$\omega$ and $A$ are the angular frequency and the amplitude of the pipe oscillations respectively. Therefore, the problem under consideration is a transient developing flow, which we assume to be laminar. A non-inertial frame of reference moving with the pipe is used and the momentum conservation equation is expressed as follows:

 

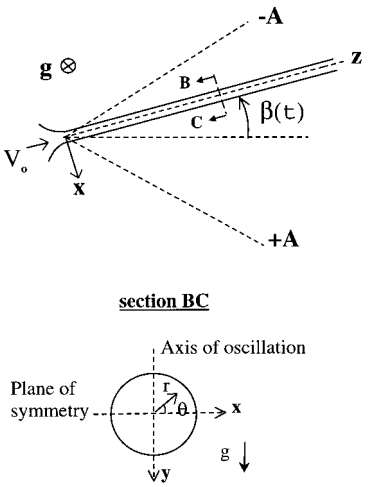


Figure 1. Schematic representation of the system under study.

$$\frac{\mathrm{D}\mathbf{V}'}{\mathrm{D}t'} = -\frac{1}{\rho}\nabla p' + g\mathbf{j} + v\nabla^2\mathbf{V}' - \frac{\mathrm{d}\Omega}{\mathrm{d}t}\times\mathbf{R} - \Omega\times(\Omega\times\mathbf{R}) - 2\Omega\times\mathbf{V} \tag{3}$$

where $\mathbf{V}'$ is the fluid velocity relative to the pipe, $\mathbf{R}$ is the position vector of a fluid particle relative to the pipe and $\rho$, $v$ are the density and kinematic viscosity of the fluid respectively. The last three terms on the right-hand side of Equation (3) represent the tangential force, the centrifugal force and the Coriolis force respectively, which are generated by the pipe oscillations.

This study is concerned with high laminar flow Reynolds numbers. Therefore, the axial diffusion terms are small compared with the corresponding terms in the transverse directions. Furthermore, as will be shown at the end of this section, the axial forces that act upstream and may cause flow reversal are smaller than the axial forces acting in the positive $z$-direction for the conditions of interest in this study. Hence, this flow field has a dominant direction and the axial momentum diffusion can be neglected [10]. This results in a set of equations that are parabolic in the $z$-direction. It should be noted that this axially parabolic model has been successfully used by many authors to study other flow problems, such as mixed convection [11], the Dean problem [12] and oscillatory flow in coiled ducts [13], which, under extreme conditions, can also result in flow reversal.

With the axially parabolic model, the pressure can be separated into two parts

$$p'(r', \theta, z', t') = p'_1(r', \theta, t') + p'_2(z', t') \tag{4}$$

The second term on the right-hand side of Equation (4) is the axial driving pressure, while the first term constitutes an in-plane perturbation.

The following non-dimensional variables are then introduced:

 

$$V_r = \frac{V'_r}{\nu/D}, \qquad V_\theta = \frac{V'_\theta}{\nu/D}, \qquad V_z = \frac{V'_z}{V_0} \tag{5a}$$

$$r = \frac{r'}{D}, \qquad z = \frac{z'}{D\,Re}, \qquad t = \frac{t'}{D^2/\nu} \tag{5b}$$

where $D$ is the pipe diameter, $V_0$ is the mean axial velocity of the fluid and $Re$ is the through-flow Reynolds number ($Re = DV_0/\nu$).

Furthermore, the centrifugal and gravitational forces have been combined with the appropriate pressure terms from Equation (4). They are non-dimensionalized with respect to $\rho V_0^2$ in the axial direction and with respect to $\rho(\nu/D)^2$ in the cross-section. This procedure gives rise to the following expressions for the non-dimensional pressures:

$$P_1(r, \theta, t) = p_1(r, \theta, t) - \frac{D^3 g}{\nu^2} r \sin\theta - \frac{1}{2} Re_\omega^2 A^2 r^2 \cos^2\theta \cos^2(Re_\omega t) \tag{6}$$

$$P_2(z, t) = p_2(z, t) - \frac{1}{2} Re_\omega^2 A^2 z^2 \cos^2(Re_\omega t) \tag{7}$$

where $Re_\omega = D^2\omega/\nu$ is the oscillation Reynolds number.

The non-dimensionalized governing equations can then be written

*Continuity:*

$$\frac{\partial V_r}{\partial r} + \frac{V_r}{r} + \frac{1}{r}\frac{\partial V_\theta}{\partial \theta} + \frac{\partial V_z}{\partial z} = 0 \tag{8}$$

*r-Momentum:*

$$\frac{\mathrm{D}V_r}{\mathrm{D}t} - \frac{V_\theta^2}{r} = -\frac{\partial P_1}{\partial r} + \left(\nabla_m^2 V_r - \frac{V_r}{r^2} - \frac{2}{r^2}\frac{\partial V_\theta}{\partial \theta}\right) - 2[Re_\omega Re\, A]V_z \cos\theta \cos(Re_\omega t) + [Re_\omega^2 Re\, A] z \cos\theta \sin(Re_\omega t) \tag{9}$$

*θ-Momentum:*

$$\frac{\mathrm{D}V_\theta}{\mathrm{D}t} + \frac{V_r V_\theta}{r} = -\frac{1}{r}\frac{\partial P_1}{\partial \theta} + \left(\nabla_m^2 V_\theta - \frac{V_\theta}{r^2} + \frac{2}{r^2}\frac{\partial V_r}{\partial \theta}\right) + 2[Re_\omega Re\, A]V_z \sin\theta \cos(Re_\omega t) - [Re_\omega^2 Re\, A] z \sin\theta \sin(Re_\omega t) \tag{10}$$

 

*z-Momentum:*

$$\frac{\mathrm{D}V_z}{\mathrm{D}t} = -\frac{\mathrm{d}P_2}{\mathrm{d}z} + \nabla_m^2 V_z + 2\left[\frac{Re_\omega}{Re} A\right](V_r \cos\theta - V_\theta \sin\theta)\cos(Re_\omega t) - \left[\frac{Re_\omega^2}{Re} A\right] r \cos\theta \sin(Re_\omega t) \tag{11}$$

where

$$\nabla_m^2 = \frac{\partial^2}{\partial r^2} + \frac{1}{r}\frac{\partial}{\partial r} + \frac{1}{r^2}\frac{\partial^2}{\partial \theta^2}$$

In the momentum equations (9)–(11) the parameters $Re_\omega Re$ and $Re\,Re_\omega^2$ indicate respectively the effect of the Coriolis force and the tangential force in the $r$–$\theta$ plane. The ratios $Re_\omega/Re$ and $Re_\omega^2/Re$ represent respectively the effect of the Coriolis force and the tangential force in the $z$-direction.

The boundary conditions for the problem under consideration are

$$V_r = V_\theta = 0, \qquad V_z = 1 \quad \text{at } z = 0 \tag{12a}$$

$$V_r = V_\theta = V_z = 0 \quad \text{at } r = 0.5 \tag{12b}$$

We also consider that the flow field is symmetrical with respect to the horizontal plane passing through the pipe centreline. Therefore

$$V_\theta = 0, \quad \frac{\partial V_r}{\partial \theta} = 0, \quad \frac{\partial V_z}{\partial \theta} = 0 \quad \text{at } \theta = 0 \quad \text{and} \quad \theta = \pi \tag{13}$$

Finally, the initial velocity field is obtained as the steady state solution of Equations (8)–(11) with boundary conditions (12) and (13) and $A = 0$.

At this point a discussion of the direction of the oscillation forces in Equations (9)–(11) is in order, as they greatly influence the flow field. As indicated in Figure 1, the pipe oscillates between two extreme positions at $\beta = -A$ and $\beta = +A$. When the pipe is moving from $\beta = -A$ towards $\beta = +A$, the angular velocity ($\Omega = \dot{\beta}$) is positive and the leading edge is at $\theta = 0$. When it is moving from $\beta = +A$ towards $\beta = -A$, the angular velocity is negative and the leading edge is at $\theta = \pi$. The centrifugal, tangential and Coriolis forces can be expressed, in Cartesian co-ordinates respectively as

$$\mathbf{F} = -\Omega \times (\Omega \times \mathbf{R}) = +\Omega^2 r \cos\theta \mathbf{x} + \Omega^2 z' \mathbf{z} \tag{14}$$

$$\mathbf{F}_t = -\frac{\mathrm{d}\Omega}{\mathrm{d}t} \times \mathbf{R} = +\omega^2 \beta z' \mathbf{x} - \omega^2 \beta x' \mathbf{z} \tag{15}$$

$$\mathbf{F}_c = -2\Omega \times V' = -2\Omega V'_z \mathbf{x} + 2\Omega V'_x \mathbf{z} \tag{16}$$

 

The cross-sectional or $x$ component of the Coriolis force acts in the opposite direction of the pipe movement provided the axial flow is in the positive direction (no flow reversal). Therefore, under this condition, this force always acts towards the trailing edge. On the other hand, the cross-sectional component of the tangential force acts towards the leading edge when the pipe is moving towards its extreme positions ($\beta = \pm A$). It acts towards the trailing edge when the pipe is moving towards its central position ($\beta = 0$). Therefore, as shown in Figure 2, the cross-sectional components of the oscillation forces act (i) in the same direction when the pipe is moving towards its central position ($\beta = 0$), and (ii) in opposite directions when the pipe is moving towards its extreme positions ($\beta = \pm A$). It should be noted that the $x$ component of the tangential force is uniform over the entire cross-section at a given instant. On the other hand, the $x$ component of the Coriolis force is not uniform over a given cross-section.

Next, consider the axial components of the oscillation forces (see Figure 2). The centrifugal force (Equation (14)) always acts in the downstream direction. Concerning the tangential force, its axial component is directed downstream in the trailing half of the pipe cross-section, and upstream in the leading half, when the pipe is moving away from $\beta = 0$. On the other hand, it is directed upstream in the trailing half of the pipe cross-section, and downstream in the leading half, when the pipe is moving towards $\beta = 0$. The direction of the axial component of the Coriolis force depends on the directions of $V'_x$ and $\Omega$. It acts downstream if $V'_x$ and $\Omega$ have the same sign, otherwise it acts upstream.

In this paragraph, the parabolic approximation used in this study is further justified. It should again be emphasized that this approximation is largely used in the literature for problems similar to the considered one [12,14,15]. Thus, many authors [16,17] have established that, for forced convection problems, the condition for the validity of the parabolic approximation is $Re \geq 400$. For the problem under study here, it was shown in the previous paragraph that the axial components of the tangential and Coriolis forces are, under some conditions, directed upstream, while the corresponding component of the centrifugal force is always

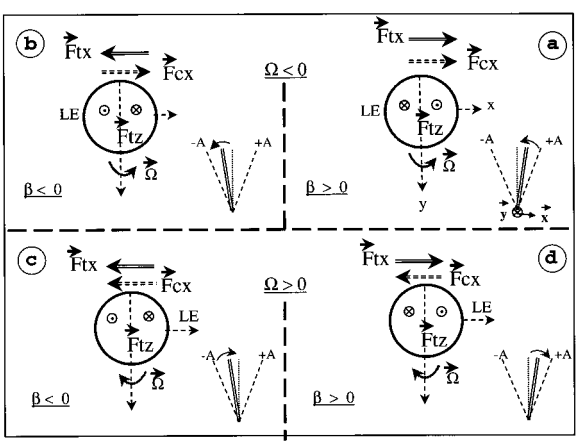


Figure 2. Direction of the tangential and Coriolis forces.

 

directed downstream. These forces are respectively proportional to $A \cdot Re_\omega/Re$, $A \cdot Re_\omega^2/Re$ (Equation (11)) and $A^2 \cdot Re_\omega^2$ (Equation (7)). For this study, both Reynolds numbers are of the same large magnitude. Therefore, the axial components of the Coriolis force ($\sim A$) and tangential force ($\sim A \cdot Re_\omega$) are negligible compared with the corresponding component of the centrifugal force ($\sim A^2 \cdot Re_\omega^2$). Hence, the possibility of flow reversal is excluded and the parabolic approximation is valid.

## 3. NUMERICAL METHOD

The governing equations (8)–(11) are solved numerically using a control volume method [18]. According to this method, a fully implicit numerical scheme is used to transform these equations to finite difference ones. The unsteady term is approximated by a backward difference, the axial advective term by an upwind difference and the diffusive and transverse convective terms by the power law scheme. The computer program is based on Patankar's procedure adapted for transient three-dimensional parabolic flows [10]. Major modifications of this procedure include (i) the implantation of the SIMPLE-C algorithm for handling the in-plane pressure–velocity coupling [19], (ii) the use of the method proposed by Raithby and Schneider [20] for the calculation of the streamwise pressure gradient $dP_2/dz$ and (iii) the adaptation necessary to handle the time-dependent terms.

As the flow field is assumed symmetrical with respect to the horizontal diameter ($\theta = 0$, $\theta = \pi$), the computation is performed only over one half of the circular cross-section.

Several different discretization grids have been tested. Table I shows the effects of the number of nodes in the $\theta$- and $r$-directions on the peripherally averaged friction factor

$$fRe = \frac{2}{\pi} \int_0^\pi \left( \frac{\partial V_z}{\partial r} \right)_{r=0.5} d\theta \tag{17}$$

Similar results for the axial pressure gradient are not presented but will be referred to. An increase of the number of nodes from 832 ($26 \times 32$ in the circumferential and radial directions respectively) to 1440 ($36 \times 40$ in the $\theta$- and $r$-directions respectively) results in a change of less than 1 per cent for the predicted values of the friction factor and of less than 2 per cent for those of the pressure gradient. In view of these and other similar results, the $26 \times 32$ grid has

Table I. Effect of cross-sectional grid on the calculated average friction factor for $Re = 500$, $Re_\omega = 1000$ and $A = 10°$.

| $z'/D$ | $26 \times 32$ | $40 \times 32$ | $36 \times 32$ | $36 \times 40$ |
|---|---|---|---|---|
| 0.10 | 62.848 | 62.848 | 62.848 | 62.404 |
| 1.00 | 28.660 | 28.664 | 28.664 | 28.620 |
| 5.20 | 19.9020 | 19.9088 | 19.9076 | 19.8814 |
| 10.25 | 18.2492 | 18.2594 | 18.2576 | 18.2354 |
| 21.05 | 17.4364 | 17.4502 | 17.4482 | 17.4266 |

 

Table II. Effect of axial grid on the calculated average friction factor for $Re = 500$, $Re_\omega = 1000$ and $A = 10°$.

| $z'/D$ | 1.02 | 3.02 | 5.02 | 12.02 | 20.50 |
|---|---|---|---|---|---|
| D1 | 28.5626 | 21.8583 | 20.0180 | 18.2992 | 17.4951 |
| D2 | 28.1751 | 21.4837 | 19.5900 | 17.8053 | 17.0310 |

been retained for subsequent calculations. It should be noted that in all these cases, the grid spacing is uniform along the circumferential direction. On the other hand, in the radial direction grid points are more closely packed near the pipe wall. Similarly, Table II shows the effects of the axial discretization on the peripherally averaged friction factor. Grid D1 consists of a non-uniform mesh with 110 cross-sections. The axial step size varies from $10^{-6}$ near the pipe entrance to $5 \cdot 10^{-4}$ near its exit. Grid D2 is obtained by halving the step size of D1. The results differ by less than 3 per cent for both the friction factor and the axial pressure gradient. For the calculations presented here grid D2 was retained. For these calculations, the CPU time is typically about 11 min per time step on an IBM RISC6000 model 375.

Several time steps have been tested to ensure that the results are accurate and independent of the time step (see Table III). A time step of $\Delta t = T/65$ has finally been chosen. $T$ is the pipe oscillation period ($T = 2\pi/Re_\omega$). The maximum resulting uncertainty is approximately $\Delta\beta/A = 0.1$ for the angular position of the pipe. The calculated results for the peripherally averaged friction factor are within 0.3 per cent of those obtained with $\Delta t = T/451$.

All grid independence tests were conducted for the case of a high oscillation Reynolds number ($Re_\omega = 1000$), which causes sharp velocity gradients. For the tests presented in Tables I, II and III, the through-flow Reynolds number is fixed at $Re = 500$ and the oscillation amplitude is $A = 10°$. Analogous grid independence tests for $Re = 1000$ gave similar results.

In each time step, the computation is marched in the $z$-direction. At each marching step, a sufficient number of iterations have been performed to ensure a converged solution. Two convergence criteria must be satisfied

- the local values of velocities at some sample points have to be converged within at least four significant digits;
- the mass balance over each control volume must be satisfied to within $10^{-4}$.

Table III. Effect of time step ($\Delta t$) on the average friction factor at $z'/D = 20.5$ for $Re = 500$, $A = 10°$ and $Re_\omega = 139$.

| $\beta$ (°) ($\Omega < 0$) | $\Delta t_1 = T/451$ | $\Delta t_2 = T/150$ | $\Delta t_3 = T/65$ |
|---|---|---|---|
| 0.0 | 16.6170 | 16.6323 | 16.6612 |
| 5.0 | 17.2453 | 17.2327 | 17.2111 |
| 9.2 | 17.2484 | 17.2349 | 17.2100 |
| 10.0 | 17.1679 | 17.1482 | 17.1130 |

 

In order to validate the computer program, we have first simulated the case of a stationary pipe. The accuracy of this solution is particularly important since, as mentioned earlier, it constitutes the initial condition for the evaluation of the transient flow field resulting from the impulsive start of the pipe oscillation at $t = 0$. These steady state results have, therefore, been compared with both analytical and experimental results from the literature. As shown in Figure 3(a), the calculated profiles for the axial velocity are very close to the corresponding measurements [21]. Similarly, Figure 3(b) shows that the axial evolution of the apparent mean friction factor, defined by Shah [22], is in excellent agreement with corresponding results by both Hornbeck [23] and Shah [22].

An additional validation of the computer code is provided for the case of a radially rotating straight pipe. Figure 4 shows that the calculated fully developed axial velocity profile is in good agreement with the corresponding measurements [24]. This result shows that the model properly accounts for the effects of the Coriolis force.

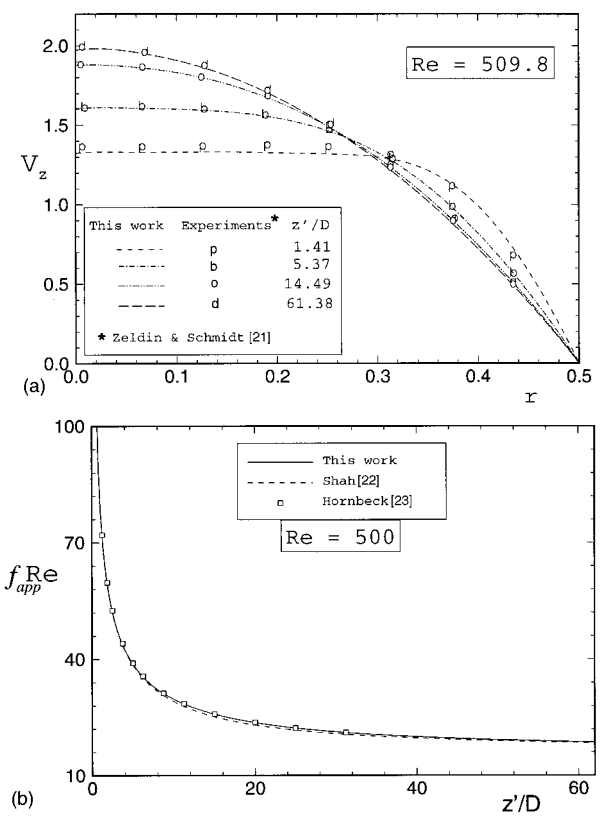


Figure 3. Validation for developing steady state flow in a stationary pipe: (a) axial velocity profile, (b) apparent mean friction factor.

 

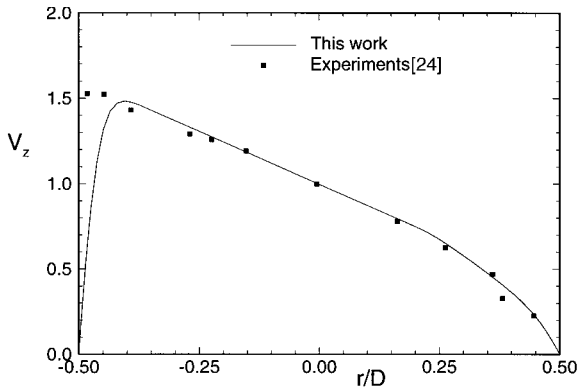


Figure 4. Validation for developed flow in a radially rotating straight pipe ($Re = 4000$ and $Re_\Omega = 1000$).

On the other hand, the validation of the transient calculations was achieved by comparing the velocity profiles in a pipe for a fluid accelerated from rest, with the corresponding analytical solution by Szymanski [25,26]. As seen in Figure 5, the agreement is excellent.

In view of these results, we consider that the adopted numerical method and the algorithm used for the calculations are reliable and accurate.

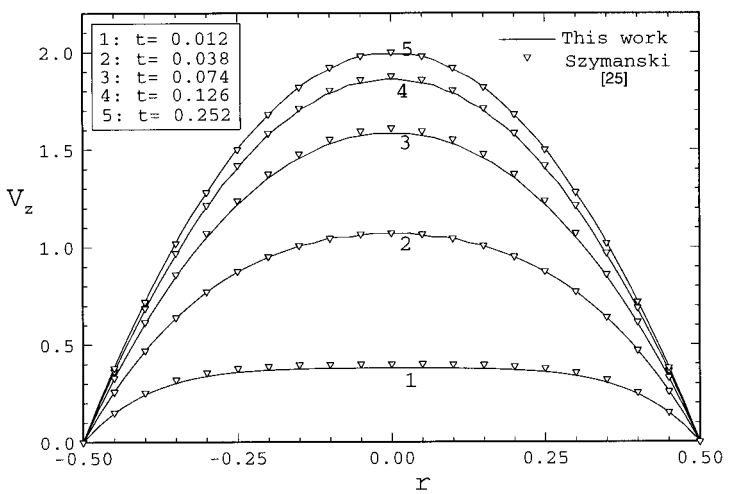


Figure 5. Validation of transient velocity profiles in a pipe for a fluid accelerated from rest.

 

## 4. RESULTS

Many simulations have been performed but, in the interest of brevity, only some selected results are presented here to describe the structure of the transient flow field during the first few cycles after the initiation of the pipe oscillations. The results presented here were calculated with $Re = 1000$, $Re_\omega = 1000$ and $A = 18°$, while the pipe length to diameter ratio was 40.46. For these values, we have established, by means of an experimental visualization, that the flow is laminar. Numerical results include the time evolutions of the different velocity components as well as those of the in-plane perturbation pressure and of the local friction coefficient $f_1$ at selected points in the flow field. The latter variable is calculated from the relation

$$f_1 Re = \left(\frac{\partial V_z}{\partial r}\right)_{r=0.5} \tag{18}$$

The results also include the time evolutions of the axial driving pressure gradient and the circumferentially averaged friction factor (Equation (17)).

### 4.1. Initiation of the secondary flow

Figures 6 and 7 show the time evolutions of the in-plane velocity vectors at $z'/D = 5.21$ and $z'/D = 40.46$ respectively, corresponding to the secondary fluid motion during the first pipe oscillation. The vectors on the upper-right-hand of each part of these figures indicate the scale for velocity vectors. At $t = 0$ (see Figures 6(a) and 7(a)) the secondary motion is purely radial and decreases with axial distance reflecting the axial development of the axisymmetric boundary layer. The modification of this initial flow field immediately after the impulsive initiation of the pipe oscillations can be understood by examining the direction and relative magnitude of the oscillation forces, which were discussed earlier.

During the first quarter of the initial oscillation when the pipe moves towards $\beta = +A$, the $x$ components of the Coriolis force is negative everywhere within the flow field (see Figure 2(d)). However, since this component of the Coriolis force is, according to Equation (16), proportional to $V_z$, its value near the pipe wall is negligible. Therefore, the fluid in the core region experiences a force in the negative $x$-direction and moves towards the pipe wall at the trailing edge. It then pushes the fluid in this region to the leading edge along the pipe wall, as seen in Figures 6(b)–(d) and 7(b)–(d). Therefore, the initial secondary flow pattern in the top half of the pipe consists of a clockwise vortex. As mentioned above, the transversal component of the tangential force is uniform over a given cross-section of the pipe at a given instant. Hence, this force can not initiate a transverse fluid movement.

It should be noted that, near the pipe entrance, the secondary flow pattern is similar to the one generated by the centrifugal force in a curved pipe [12] (Dean's problem). The essential difference between these two flow fields is due to the fact that, in the present case, the intensity of the vortices is time-dependent. Further downstream, however, the present case secondary flow is much more complex. Thus, the velocity profile along a given radius exhibits local minima and an additional weak vortex appears near the trailing edge (see Figure 7(f) and (m)).

 

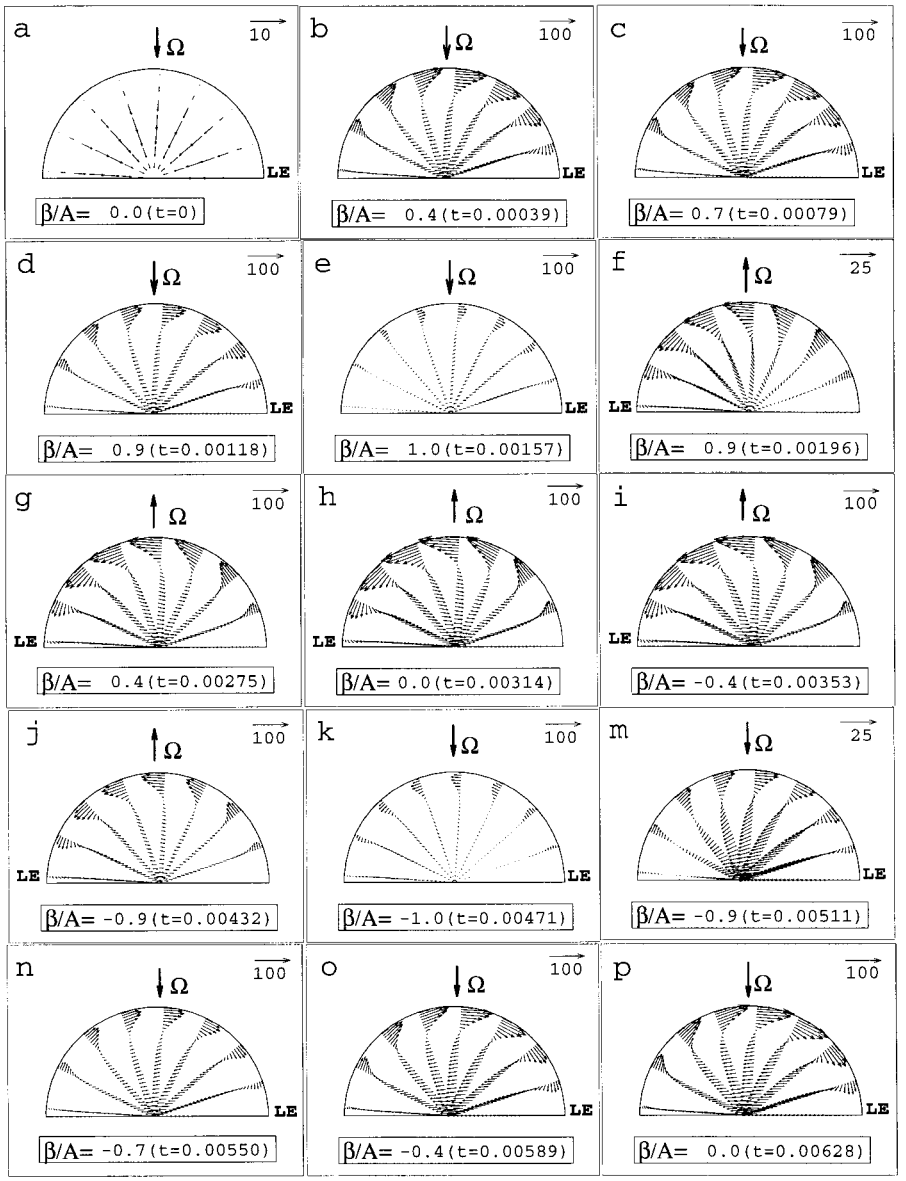


Figure 6. Secondary flow pattern at $z'/D = 5.21$ during the first tube oscillation.

Figures 6 and 7 also show that when the pipe reaches its extreme position at $\beta = +A$ (Figures 6(e) and 7(e)), the clockwise vortex in the upper half of the pipe is still present, albeit less important than at earlier instants. The secondary velocity vectors do not become zero until

 

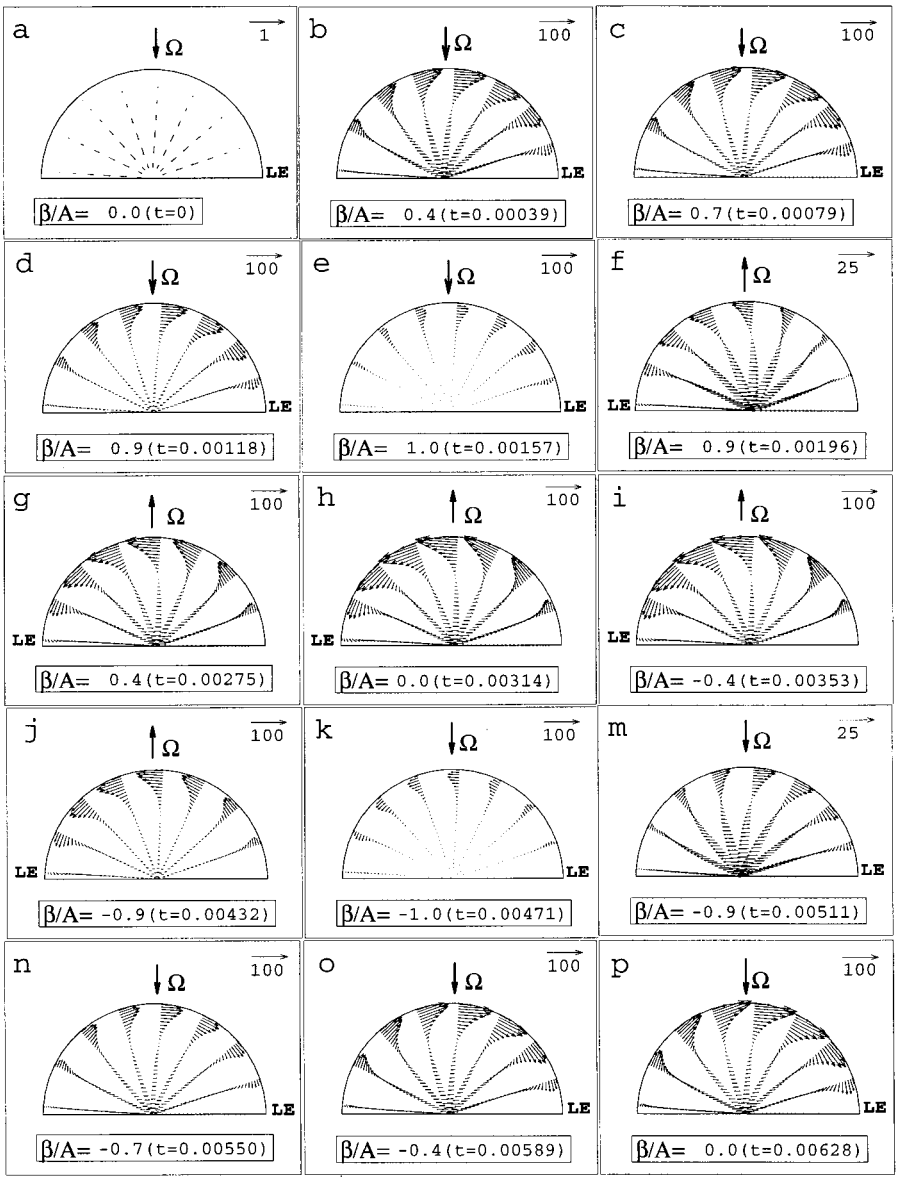


Figure 7. Secondary flow pattern at $z'/D = 40.46$ during the first tube oscillation.

some later time (corresponding to intermediate positions between Figures 6(e) and (f) and 7(e) and (f)) when the pipe has started moving back towards $\beta = 0$. Thus, owing to inertial effects, the secondary motion of the fluid lags behind the pipe oscillations.

 

A final point of interest arising from Figures 6 and 7 is the apparent symmetry of the secondary flow patterns for instants differing by half a pipe oscillation period (see, for example, Figures 6(d) and (j) or 7(f) and 7(m)). This point is addressed in detail later.

### *4.2. Transient evolution of the axial velocity*

Figure 8 shows the time evolution of the axial velocity at point $M$ ($\theta = 0$, $r = 0.25$) for three different axial positions during the first four pipe oscillations. The initial values of $V_{zM}$ at $t = 0$ (i.e. when the pipe is at rest at $\beta = 0$) correspond to the steady state solution discussed earlier (see Figure 3). An analysis of the axial components of the tangential and Coriolis forces explains the initial variation of the axial velocity shown in this figure. Thus, at $t = 0$, the pipe is at $\beta = 0$; therefore, according to Equation (15), the axial component of the tangential force is zero. At that instant, $\Omega$ is positive and maximum, while for the point $M$ ($\theta = 0$, $r = 0.25$) under consideration, the velocity in the $x$-direction is negative, as it is due to the boundary layer growth and is, therefore, directed towards the centre of the pipe. Thus, according to Equation (16), the axial component of the Coriolis force at $t = 0$ is negative. This explains the fact that the axial velocity at $M$ decreases immediately after the pipe oscillation is initiated at $t = 0$. Later, as the pipe moves towards $\beta = +A$ and then back towards $\beta = 0$, the sum of the axial components of the tangential and Coriolis forces is continuously negative. Therefore, the acceleration of $V_z$ observed in Figure 8 as the pipe approaches $\beta = 0$ cannot be explained on this basis. It is rather a result of the complex interaction between these axial forces, the axial pressure gradient and the coupling between the axial and in-plane motions.

It should be noted that $V_{zM}$ at $z'/D = 5.21$ reaches its extreme values when the pipe is at $\beta \approx 0$. Further downstream, however, for $z'/D = 11.21$ and $z'/D = 40.46$, for example, the extreme values of the axial velocity at $M$ occur earlier than the central angular position of the pipe. As indicated by these results, the time lag between the occurrence of the extreme values of $V_{zM}$ and $\beta$ decreases with increasing distance from the pipe entrance.

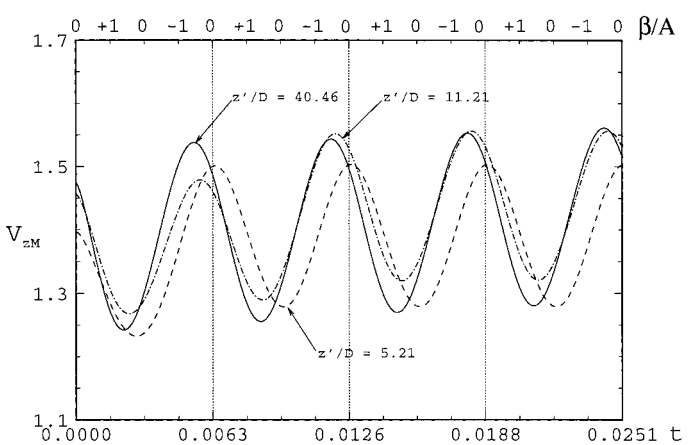


Figure 8. Time evolution of the axial velocity at point $M$ ($\theta = 0$, $r = 0.25$).

 

Figure 8 also shows that during the first pipe oscillation, the extreme values of the axial velocity differ from the corresponding values for subsequent oscillations. Furthermore, the corresponding amplitude is greatest at $z'/D = 40.46$ and smallest at $z'/D = 11.21$, while the average value increases monotonically with axial distance. On the other hand, during the fourth pipe oscillation, the amplitude of $V_{zM}$ increases monotonically with $z$, while its average value is greatest at $z'/D = 11.21$. This complicated behaviour is attributed to the fact that point $M$ is situated in the central core region at $z'/D = 5.21$ and in the boundary layer at $z'/D = 40.46$.

The evolution of the axial velocity profile along the horizontal diameter at $z'/D = 5.21$ is shown in Figure 9 for different instants during the first pipe oscillation. The circles define the

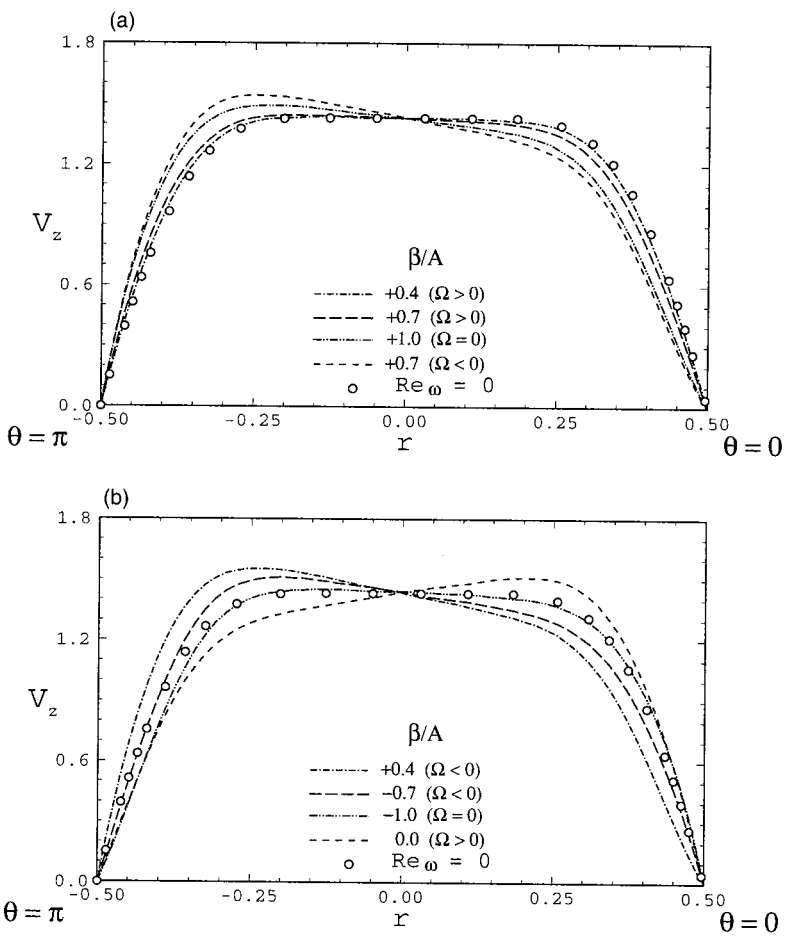


Figure 9. Time evolution of the axial velocity profile at $z'/D = 5.21$ along the horizontal diameter ($\theta = 0$, $\theta = \pi$) during the first pipe oscillation.

 

corresponding velocity profile for a stationary pipe (cf. Figure 3), which is also the initial velocity profile at $t = 0$ for the transient problem under study. As the pipe moves from $\beta = 0$ towards $\beta = +A$, the axial velocity near the leading edge ($\theta = 0$) decreases while it increases near the trailing edge ($\theta = \pi$) in order to satisfy the mass conservation equation. This behaviour is obviously due to the fluid inertia, which prevents it from following the impulsive initiation of the pipe movement at $t = 0$. It is important to note that this tendency continues even after the pipe has started moving back towards $\beta = 0$. Thus, the maximum distortion of this velocity profile during the first pipe oscillation occurs when $\beta/A = +0.4$ and the pipe is moving towards $\beta = 0$ ($\Omega < 0$). Then, as the pipe movement continues beyond $\beta = 0$ towards $\beta = -A$, the lack of symmetry diminishes and for $\beta = -A$, the velocity profile is almost identical to that for a stationary pipe. Finally, when the pipe reaches once again the position $\beta = 0$, the axial fluid velocity near the leading edge ($\theta = 0$) is higher than that near the trailing edge. The distortion of the velocity profile during this first pipe oscillation can be quantified by the ratio of its maximum value to the velocity on the axis of a stationary pipe. In the case of Figure 9, this ratio is equal to 1.07.

The corresponding evolutions of the axial velocity profile at $z'/D = 11.21$ and $z'/D = 40.46$ are qualitatively similar to those of Figure 9. However, the ratio quantifying the distortion of the profile decreases with axial distance: its value is 1.04 at $z'/D = 11.21$ and 1.01 at $z'/D = 40.46$. The latter value indicates that, far from the entrance, where the velocity profile for a stationary pipe is quasi-parabolic, the maximum velocity during the pipe oscillation does not change much, although its position oscillates around the longitudinal axis of the pipe.

### *4.3. Evolution of some local variables*

Figure 10 shows the time evolution of the in-plane pressure $P_1$ (see Equation (6)) and of the circumferential velocity $V_\theta$ at a particular point $Q$ ($\theta = 2.16$ rad, $r = 0.462$) for three different axial positions. This pressure is closely related to the secondary motion depicted in Figures 6 and 7. For the particular point $Q$, which is in the upper left quadrant of the cross-section, this pressure decreases when the pipe is moving from $\beta = -\mathrm{A}$ towards $\beta = +\mathrm{A}$ and increases when the pipe is moving in the opposite direction. For $z'/D = 40.46$, the extreme values of this variable occur when $\beta \approx \pm A$. As $z'/D$ decreases, these extreme values occur later. Therefore, as is the case for $V_{zM}$, the time lag between the occurrence of the extreme values of $P_{1Q}$ decreases with increasing axial distance. The extreme values of $P_{1Q}$ are essentially the same for all cycles, including the first. This is not the case for $V_{\theta Q}$ for which the extreme values during the first pipe oscillation are quite different from the corresponding values for subsequent oscillations. Contrary to the case of $V_{zM}$ (see Figure 8), the extreme values of $V_{\theta Q}$ occur when the tube is very close to $\beta = 0$ and the influence of axial distance on the phase difference between the oscillations of $V_{\theta Q}$ and $\beta$ is negligible.

The influence of axial distance on the amplitudes of $P_1$ and $V_{\theta Q}$ during the fourth pipe oscillation is qualitatively and quantitatively different. Both these amplitudes increase with axial distance. However, on the basis of the results of Figure 10, the amplitude of $P_1$ increases linearly with the axial distance, while that of $V_{\theta Q}$ increases very rapidly near the pipe entrance and then tends towards an asymptotic value that is independent of the axial distance.

 

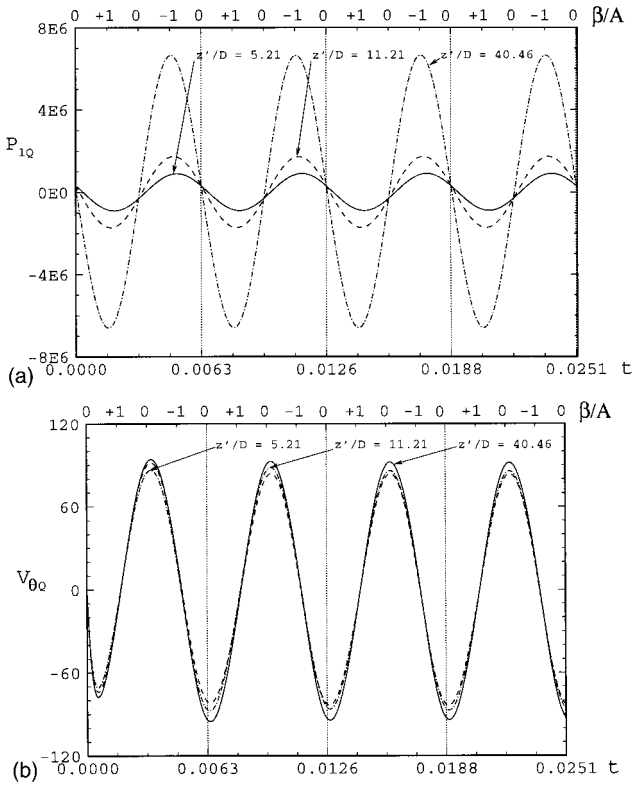


Figure 10. Time evolution of (a) the in-plane pressure $P_1$, and (b) the circumferential velocity $V_\theta$ at point $Q$ ($\theta = 2.16$ rad, $r = 0.462$).

Figure 11 shows the time evolution of the local friction coefficient at $\theta = 0$, which is closely related to the axial velocity profile of Figure 9 as it is calculated from Equation (18). Its extreme values occur later than the extreme positions of the pipe. The time lag between the extreme pipe positions and the extreme values of this coefficient increases slightly with axial distance. Its average value decreases with axial distance while its amplitude is essentially independent of $z$. The corresponding evolution for the local friction coefficient at $\theta = \pi$ can be deduced from the velocity profiles of Figure 9. The values for $\theta = 0$ and $\theta = \pi$ are exactly the same at $t = 0$, but the latter initially increases, reaches a maximum for $\beta/A = +0.8$ ($\Omega < 0$) and then decreases. The phase difference between the local friction coefficient at these two positions ($\theta = 0$ and $\theta = \pi$) is approximately half of the pipe oscillations period. On the other hand, the maximum and minimum values of these two local friction factors are not the same during the first tube oscillation because of the lack of symmetry of the axial velocity profile.

In order to quantify the effects of the pipe oscillations on the flow field, especially during the first pipe oscillation, the extreme values of some flow variables are given in Table IV. For local

 

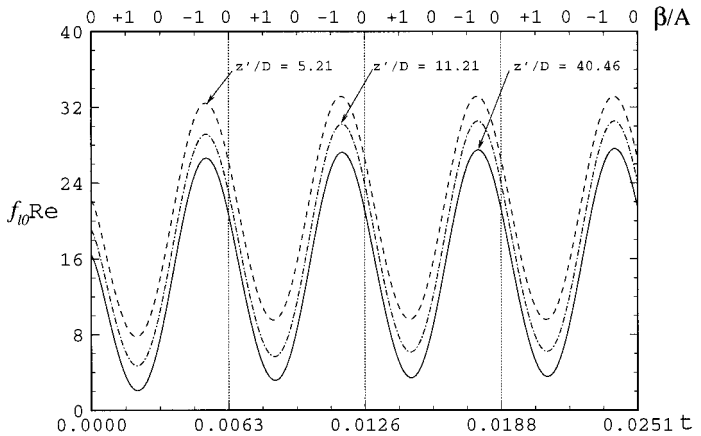


Figure 11. Time evolution of the local friction factor at $\theta = 0$.

Table IV. Relative difference of the extreme values of some flow variables during the first pipe oscillation with respect to the corresponding value for a stationary pipe.

| $z'/D$ | 5.21 | | 11.21 | | 40.46 | |
|---|---|---|---|---|---|---|
| $V_{zM}$ (%) | 7.4 | −11.8 | 1.4 | −13.0 | 4.2 | −15.8 |
| $f_{l0}\,Re$ (%) | 46.2 | −64.8 | 53.1 | −75.1 | 62.4 | −87.1 |
| $f\,Re$ (%) | 5.4 | 1.4 | 6.6 | 2.0 | 8.2 | 3.0 |
| $dP_2/dz$ (%) | 3.0 | 1.6 | 5.3 | 1.1 | 7.8 | 2.8 |

characteristics, the effect is significant. Thus, at $z'/D = 5.21$, the maximum and minimum values of $V_{zM}$ during the first pipe oscillation are respectively 7.4 and $-11.8$ per cent different from the corresponding values for a stationary pipe. For the fourth pipe oscillation, these differences are respectively 7.5 and $-8.5$ per cent (see Figure 8). In the case of the local friction factor at $\theta = 0$ ($f_{l0}Re$), which differs by more than $\pm 45\%$ from the corresponding stationary pipe results, the effect is more dramatic. These large variations of $f_{l0}Re$ are due to the fact that the point under consideration ($\theta = 0$, $r \approx 0.5$) is alternatively located at the leading and at the trailing edges. On the other hand, the effect of the oscillations on global flow characteristics, such as the peripherally averaged friction factor ($fRe$) and the mean axial pressure gradient ($dP_2/dz$), is less important but not negligible.

### 4.4. Periodic regime

The results of Figures 8, 10 and 11 clearly suggest that after the initial two or three pipe oscillations, the flow field becomes periodic. This has been firmly established by comparing the values of several variables at time intervals equal to the pipe oscillation period. Thus, Table V

 

shows that at $z'/D = 11.21$ there is no variation whatsoever of any of the six variables after the fourth pipe oscillation; in fact, the difference between corresponding values at $t = 3T$ and $t = 4T$ is in all cases less than 0.1 per cent of the former values. The same levels of confidence for the existence of periodicity are obtained earlier at $z'/D = 5.21$. Thus there is no variation whatsoever of any of the six variables after the third pipe oscillation, while the difference between corresponding values at $t = 2T$ and $t = 3T$ is in all cases less than 0.1 per cent. On the other hand, at $z'/D = 40.46$, the convergence towards the periodic flow regime takes much longer: the values for $P_1$ ($\theta = 0.06$, $r = 0.256$) differ by 3 per cent between $t = 5T$ and $t = 6T$. However, all the other variables differ by less than 1 per cent between these two instants and the tendency towards the existence of an established periodic flow regime is clear even at this distance from the entrance.

### 4.5. Flow resistance

The time evolutions of the peripherally averaged friction factor, calculated from Equation (17), and of the axial pressure gradient are shown in Figures 12 and 13 respectively. The established periodic regime following the initial transient period is again evident. Both the friction factor and the absolute value of the axial pressure gradient decrease with increasing axial distance. Their values are always higher than those for a stationary pipe, which correspond to the instant $t = 0$. Thus, the pipe oscillation and the ensuing secondary motion increase the losses over and above those for a stationary pipe, as illustrated by the values in Table IV.

It should be noted that the amplitude of the oscillations for both $fRe$ and $\mathrm{d}P_2/\mathrm{d}z$ increases with axial distance. On the other hand, the time lag between the extreme values of these two variables and the extreme positions of the pipe are essentially independent of axial position.

Figures 12 and 13 exhibit an interesting characteristic, which was not present in any of the previous figures: the average friction factor and the axial pressure gradient exhibit two maxima and two minima within a single pipe oscillation. Close to the pipe entrance, at $z'/D = 5.21$, for example, consecutive maxima during the fourth pipe oscillation have the same value to within 0.003 per cent; the same is true for the corresponding consecutive minima. This observation suggests that the established periodic oscillations for $\boldsymbol{f}$ and $\mathrm{d}P_2/\mathrm{d}z$ have half the period of the pipe movement. This point of view is reinforced by the apparent symmetry of the secondary

Table V. Evolution of different flow variables at $z'/D = 5.21$ for $Re = 1000$, $Re_\omega = 1000$ and $A = 18°$.

| $t$ | 0 | $T$ | $2T$ | $3T$ | $4T$ | $5T$ |
|---|---|---|---|---|---|---|
| $V_z$ ($\theta = 0$, $r = 0.256$) | 1.4567 | 1.4595 | 1.5277 | 1.5313 | 1.5313 | 1.5313 |
| $f_1 Re$ ($\theta = 0$) | 19.0646 | 23.0800 | 23.9540 | 24.1200 | 24.1240 | 24.1240 |
| $\mathrm{d}P_2/\mathrm{d}z$ | −44.124 | −45.839 | −45.731 | −45.737 | −45.739 | −45.739 |
| $f Re$ | 19.0646 | 20.1440 | 20.1680 | 20.1700 | 20.1700 | 20.1700 |
| $V_\theta$ ($\theta = 2.16$, $r = 0.462$) | −5.2191E−12 | −87.167 | −85.493 | −86.318 | −86.351 | −86.352 |
| $P_1$ ($\theta = 0.06$, $r = 0.256$) | 4.0666E+03 | −5.0513E+03 | −7.6835E+03 | −7.9663E+03 | −7.9723E+03 | −7.9723E+03 |

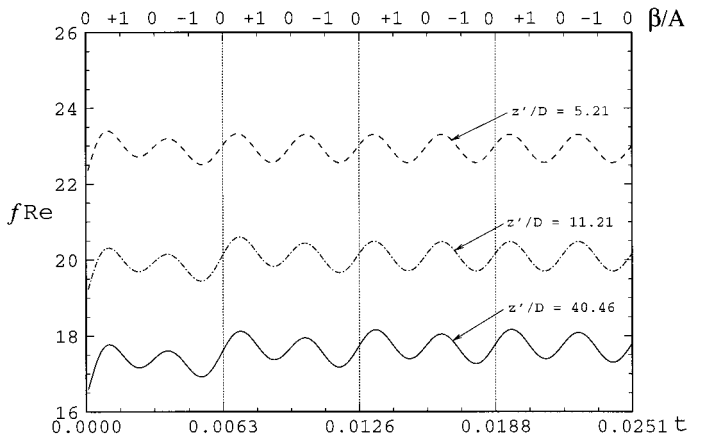


Figure 12. Time evolution of the circumferentially averaged friction factor.

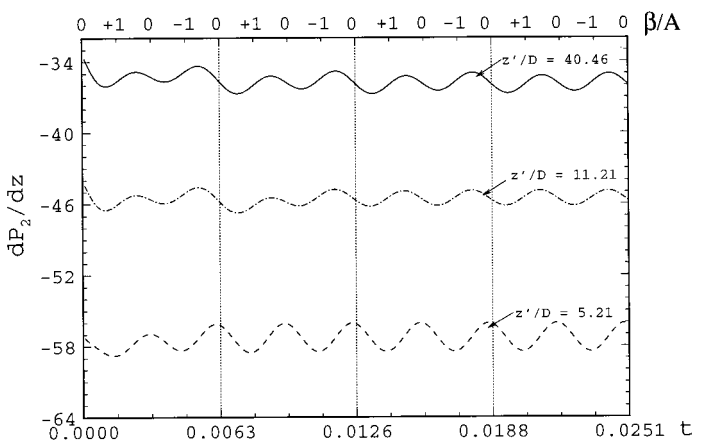


Figure 13. Time evolution of the axial pressure gradient.

velocity field for instants differing by half the pipe oscillation period, which is obvious even during the first pipe oscillation (see Figure 6(d) and (j) or (g) and (o)). The symmetry of the entire flow field for instants differing by half a pipe oscillation period seems entirely plausible during the established periodic flow regime and would explain the fact that the average friction factor seems to oscillate with twice the frequency of the pipe movement. A detailed examination of Figures 12 and 13 reveals that, far from the entrance, the differences between two consecutive maxima (and minima) during the fourth pipe oscillation are always less than 0.5

 

per cent. At this point, therefore, we ascertain that the frequency of the two variables shown in Figures 12 and 13 is indeed twice that of the pipe oscillations.

### 4.6. *Effects of the pipe oscillation pattern*

The results presented in the previous sections were obtained for the pipe oscillation pattern defined by Equations (1) and (2) (case 1). However, results have also been calculated for two other oscillation patterns described by the following relations:

Case 2

$$\beta = -A\,\sin(\omega t') \quad \text{and} \quad \Omega = -A\omega\,\cos(\omega t')\mathbf{y} \tag{19}$$

Case 3

$$\beta = A\,\cos(\omega t') \quad \text{and} \quad \Omega = -A\omega\,\sin(\omega t')\mathbf{y} \tag{20}$$

For both cases 1 and 2, the pipe starts its oscillations at $\beta = 0$. It is initially moving towards $\beta = +\mathrm{A}$ in case 1 ($\Omega > 0$) and towards $\beta = -\mathrm{A}$ in case 2 ($\Omega < 0$). In case 3, the pipe starts its oscillations at $\beta = +\mathrm{A}$. In all three cases, the values of the flow parameters are the same: $A = 18°$ and $Re = Re_{\omega} = 1000$.

Figures 14 and 15 illustrate the effects of the pipe oscillation pattern on selected flow variables presented previously for the base case (case 1). The transient effect of these oscillation patterns is clear from these figures. Thus, during the first pipe oscillation the evolutions of $V_{zM}$ are quite different (Figure 14), although these three cases differ by a simple phase difference (see Equations (2), (19) and (20)). The evolution of $V_{zM}$ for case 1 has been explained in Section 4.2. A similar analysis explains the evolution for the other two cases. The first extreme values of $V_{zM}$ at $z'/D = 40.46$ for cases 1, 2 and 3 differ from the corresponding value for a stationary pipe by $-15.7$, $+13.6$ and $+14.9$ per cent respectively. These observations clearly indicate that the oscillation pattern influences the transient flow regime. Figure 14(b) suggests that it also influences the duration of the transient regime. On the other hand, once the periodic regime has been established (i.e. for the fourth pipe oscillation at $z'/D = 5.21$), the evolution of $V_{zM}$ for each of the three cases is the same except for a phase difference (Figure 14(a)).

Figure 15 shows the time evolution of the mean friction factor ($fRe$) for the three pipe oscillation patterns. The behaviour of $fRe$ for cases 1 and 2 is identical, while it is quite different for case 3, especially during the first pipe oscillation. At $z'/D = 40.46$, the first maxima of $fRe$ for cases 1 and 3 are respectively 8 and 12 per cent higher than from the corresponding value for a stationary pipe. The corresponding values of the first minima are respectively 3 and 7 per cent higher than the value for a stationary pipe. The effect of the pipe oscillation pattern on $fRe$ is more important at the pipe exit ($z'/D = 40.46$) than at the pipe entrance. Indeed, the oscillation forces are more important at the pipe exit (see Equations (9) and (10)).

 

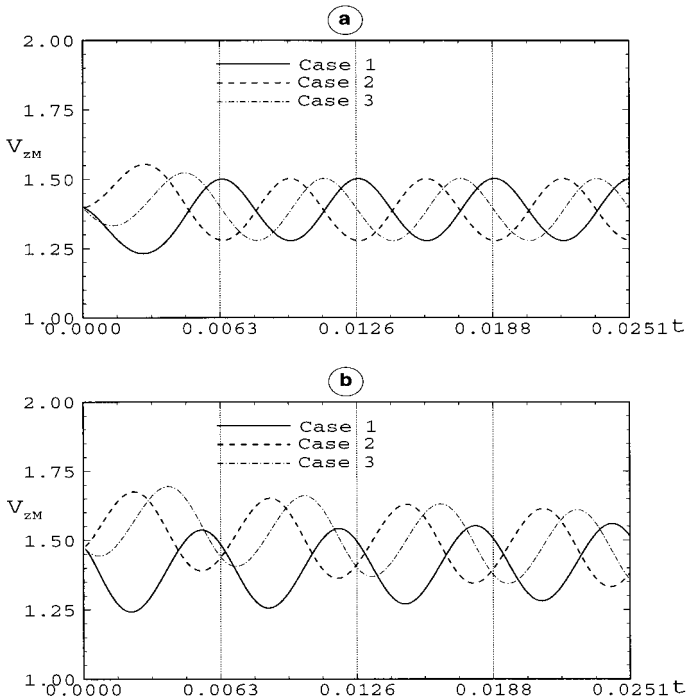


Figure 14. Comparison of the axial velocity evolution at point $M$ ($\theta = 0$, $r = 0.25$) for three different pipe oscillation patterns at (a) $z'/D = 5.21$ and (b) $z'/D = 40.46$.

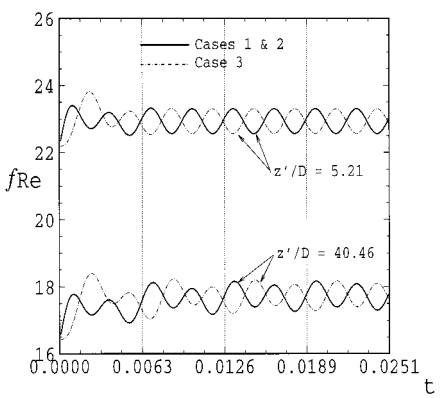


Figure 15. Comparison of the circumferentially averaged friction factor evolution for three different pipe

 

## 5. CONCLUSION

The interaction between the developing laminar flow in a straight horizontal pipe and the impulsively initiated oscillations of the latter around the vertical diameter at its entrance has been studied numerically. It is believed that the computations presented here are the first of their kind. The inertial forces acting on the fluid generate a pulsating flow, which is characterized by a pair of counter-rotating vortices symmetrical about the horizontal plane through the longitudinal axis of the pipe. These vortices are alternatively clockwise and anti-clockwise. Their intensity varies with both time and axial distance. This secondary flow influences the axial velocity profile, which is no longer axisymmetric. Thus, the position of the axial velocity maximum oscillates along the horizontal diameter of the pipe. Its value near the tube entrance is higher than that for a stationary pipe while far downstream, these two maxima are essentially the same. All local flow variables (velocity components, pressure and local wall shear stress) oscillate with the same frequency as the pipe. After an initial transient regime all these oscillations became periodic. The duration of this transient regime increases with axial distance. This duration also depends on the pipe oscillation pattern. On the other hand, average variables (such as the axial pressure gradient and the peripherally averaged friction factor) exhibit two maxima and two minima during a single pipe oscillation. After the transient regime, these variables oscillate with twice the frequency of the pipe oscillations.

ACKNOWLEDGMENTS

The authors wish to thank the Natural Sciences and Engineering Research Council of Canada for its financial support.

REFERENCES

1. Morris WD. *Heat Transfer and Fluid Flow in Rotating Coolant Channels*. Research Studies Press, Wiley: New York, 1981.
2. Soong CY, Lin ST, Hwang GJ. An experimental study of convective heat transfer in radially rotating rectangular ducts. *ASME Journal of Heat Transfer* 1991; **113**: 604.
3. Fann S, Yang W-J. Hydrodynamically and thermally developing laminar flow through rotating channels having isothermal walls. *Numerical Heat Transfer Part A* 1992; **22**: 257.
4. Kurwzeg UH, Chen J. Heat transfer along an oscillating flat plate. *ASME Journal of Heat Transfer* 1988; **110**: 789.
5. Kazakia JY, Rivlin RS. The influence of vibration on Poiseuille flow of a non-Newtonian fluid. *Rheologica Acta* 1978; **17**: 210.
6. Maloy KJ, Goldburg W. Measurements on transition to turbulence in a Taylor–Couette cell with oscillatory inner cylinder. *Physics of Fluids A* 1993; **5**: 1438.
7. Berman J, Mockros LF. Flow in a rotating non-aligned straight pipe. *Journal of Fluid Mechanics* 1984; **144**: 297.
8. Benhamou B, Galanis N, Laneville A. Laminar flow in a tube subject to sinusoidal oscillations. In *ECCOMAS'98*, Athens, Greece, vol. 1, Papailiou K (ed.). Wiley: New York, 1998; 1302.
9. Benhamou B, Galanis N, Laneville A. Numerical study of laminar incompressible flow in an oscillating tube. In *CSME'98 Forum*, Toronto, Canada 19–22 May, vol. 1, Rosen MA, Naylor D, Kawall JG (eds). Ryerson Polytechnic University: Toronto, 1998; 169.
10. Patankar SV, Spalding DB. A calculation procedure for heat, mass and momentum transfer in three-dimensional parabolic flows. *International Journal for Heat and Mass Transfer* 1972; **15**: 1787.
11. Ouzzane M, Galanis N. Developing mixed convection flow in an inclined tube under circumferentially non-uniform heating at outer surface. *Numerical Heat Transfer Part A* 1999; **35**: 609.

 

12. Bara B, Nandakumar K, Masliyah JH. An experimental and numerical study of the Dean problem: flow development towards two-dimensional multiple solutions. *Journal of Fluid Mechanics* 1992; **244**: 339.
13. Ravi Sankar S, Nandakumar K, Masliyah JH. Oscillatory flows in coiled square ducts. *Physics of Fluids* 1988; **31**: 1348.
14. Pollard A. The numerical calculation of partially elliptic flows. *Numerical Heat Transfer* 1979; **2**: 267.
15. Cheng CH, Weng CJ, Aung W. Buoyancy effect on the flow reversal of three-dimensional developing flow in a vertical rectangular duct. A parabolic model solution. *ASME Journal of Heat Transfer* 1995; **117**: 238.
16. Shah RK, London AL. *Laminar Flow Forced Convection in Ducts*. Academic Press: New York, 1978.
17. Pagliarini G. Steady laminar heat transfer in the entry region of circular tubes with axial diffusion of heat and momentum. *International Journal for Heat Mass Transfer* 1989; **32**: 1037.
18. Patankar S. *Numerical Heat Transfer and Fluid Flow*. McGraw-Hill: New York, 1980.
19. Van Doormaal JP, Raithby GD. Enhancements of the SIMPLE method for predicting incompressible fluid flows. *Numerical Heat Transfer* 1984; **7**: 147.
20. Raithby GD, Schneider GE. Numerical solution of problems in incompressible fluid flow: treatment of the velocity–pressure coupling. *Numerical Heat Transfer* 1979; **3**: 417.
21. Zeldin B, Schmidt FW. Developing flow with combined forced-free convection in an isothermal vertical tube. *ASME Journal of Heat Transfer* 1972; **94**: 211.
22. Shah RK. A correlation for laminar hydrodynamic entry length solutions for circular and non-circular ducts. *ASME Journal of Fluids Engineering* 1978; **100**: 177.
23. Hornbeck RW. Laminar flow in the entrance region of a pipe. *Applied Science Research Section A* 1964; **13**: 224.
24. Ito H, Nanbu K. Flow in rotating straight pipes of circular cross section. *ASME Journal of Basic Engineering* 1971; **93**: 383.
25. Szymanski P. Quelques solutions exactes des équations de l'hydrodynamique du fluide visqueux dans le cas d'un tube cylindrique. *Journal de mathématiques pures et appliquées Série 9* 1932; **11**: 67.
26. Schlichting H. *Boundary Layer Theory*. McGraw Hill: New York, 1979.

 